Exceptional thermoelectric performance in AB_2Sb_2-type Zintl phases through band shaping

Jingdan Lei[1], Hexige Wuliji[1], Qingyong Ren[2,3], Xiaowen Hao[2,3], Hongliang Dong[4], Heyang Chen[1], Tian-Ran Wei[1,5], Jiawei Zhang[6], Pengfei Qiu[6], Kunpeng Zhao[1,5], and Xun Shi[1,6]**

Calculation of the effective mass m^*

The effective mass of the holes at the valence band maximum along different directions m_{xx}^*, m_{yy}^* and m_{zz}^* are calculated according to the definition of effective mass by solving the second derivative of energy and k points. Then the effective mass m_b^* of a single band (VB1 or VB2) can be calculated by[1, 2]:

$$m_b^* = \left(m_{xx}^* \times m_{yy}^* \times m_{zz}^*\right)^{\frac{1}{3}}.$$

The derived values are listed in **Table S1**.

Three different models of the Rietveld refinement

Given that $YbZn_2Sb_2$ has a similar crystal structure as that of Mg_3Sb_2, we here consider three different models to assess the alloying effect of Yb/Zn in Mg_3Sb_2: (i) Zn and Yb respectively replace Mg2 (2*d*) and Mg1 (1*a*) positions (**Figure S13a**); (ii) Zn and Yb randomly reside on both Mg1 and Mg2 positions (**Figure S13b**); (iii) Yb reside only on the Mg2 (2*d*) while Zn could distribute on both Mg1 (1*a*) and Mg2 (2*d*) positions (**Figure S13c**). **Figure S13d-f** shows the Rietveld refinements with these three models for the exemplary $(Mg_3Sb_2)_{0.6}(YbZn_2Sb_2)_{0.4}$. When the atom occupancy is fixed, model (i) shows much lower good goodness-of-fit χ^2 (1.7274) and lower residuals in the profile compared to model (ii) (χ^2 = 5.0911) and model (iii) (χ^2 = 9.7873), indicating that model (i) is more plausible. When the atom occupancy is relaxed, model (iii) could also give a good fit (χ^2 = 1.7216). However, such model leads to a Zn occupancy of less than zero and an Mg occupancy of more than one at the 1*a* position, which is physically meaningless (**Figure S14**). Therefore, it can be determined

that Yb occupy 1*a* position along with Mg1 and Zn share the $2d_1$ position with Mg2. The lattice parameters derived from Rietveld refinement are listed in **Table S2** and **S3**.

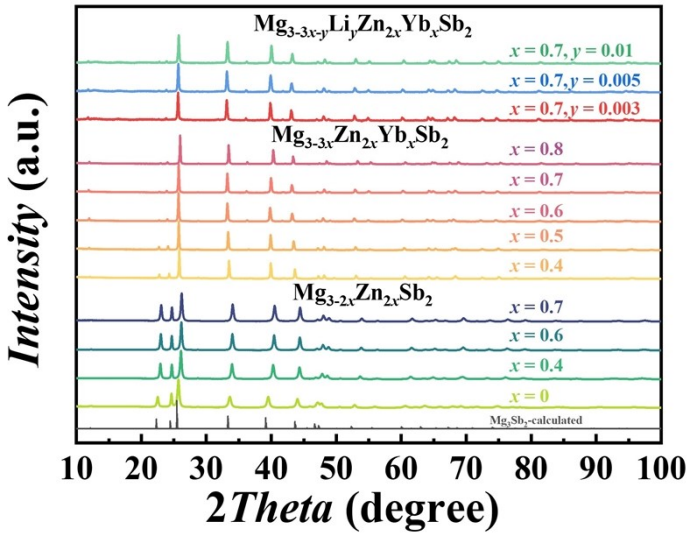

Figure S1. XRD patterns of $Mg_{3-2x}Zn_{2x}Sb_2$ (x = 0, 0.4, 0.6, 0.7), $Mg_{3-3x}Zn_{2x}Yb_xSb_2$ (x = 0.4, 0.5, 0.6, 0.7, 0.8), and $Mg_{3-3x-y}Li_yZn_{2x}Yb_xSb_2$ (x = 0.7; y = 0.003, 0.005, 0.01). All the diffraction peaks of $Mg_{3-2x}Zn_{2x}Sb_2$ samples are indexed to the same trigonal structure with Mg_3Sb_2. For the Zn/Yb co-alloyed samples, the crystal symmetry is well maintained but the relative peak intensity and peak position are obviously changed.

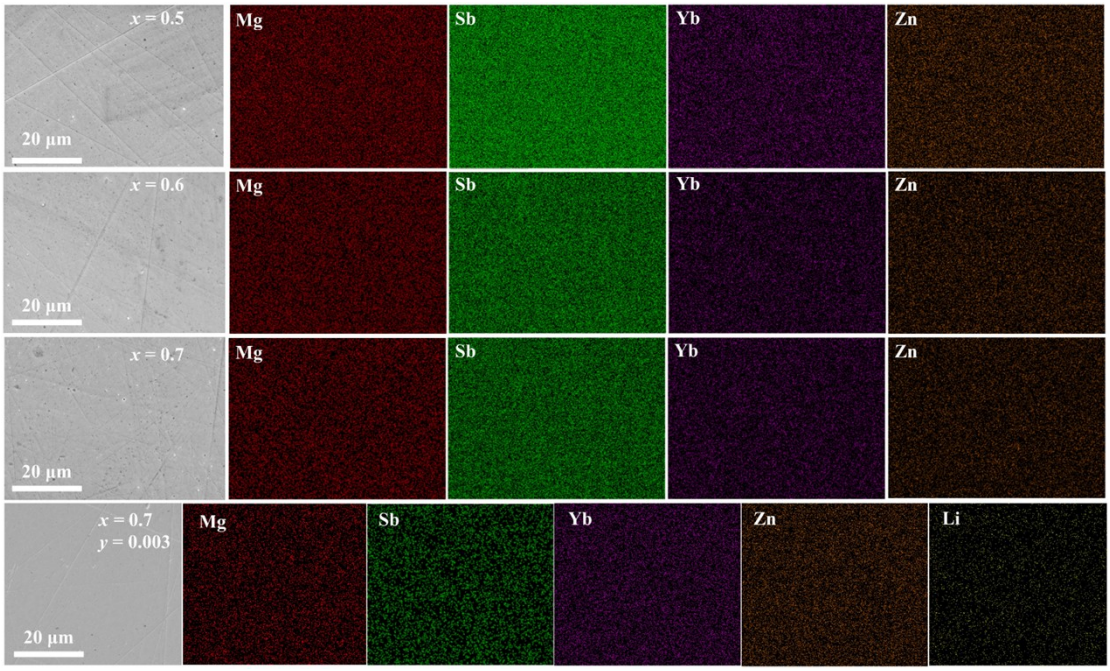

Figure S2. Back scattering electron (BSE) images and corresponding energy dispersive

spectroscopy (EDS) mappings for $Mg_{3-3x}Zn_{2x}Yb_xSb_2$ (x = 0.5, 0.6, 0.7) and $Mg_{3-3x-y}Li_yZn_{2x}Yb_xSb_2$ (x = 0.7; y = 0.003) samples, which shows that all elements are homogeneously distributed in the sintered samples, implying the formation of pure solid solutions.

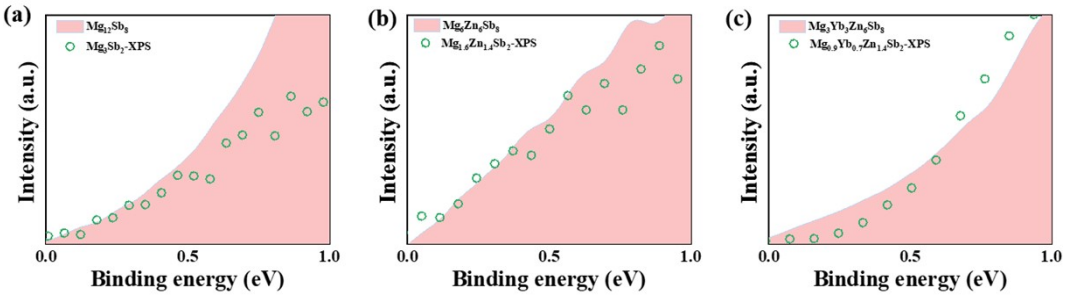

Figure S3. A comparison of X-ray photoemission spectroscopy (XPS) valence band (VB) spectrum for pristine Mg_3Sb_2, $Mg_{1.6}Zn_{1.4}Sb_2$, and $Mg_{0.9}Zn_{1.4}Yb_{0.7}Sb_2$ and calculated density of states (DOS) for $Mg_{12}Sb_8$, $Mg_6Zn_6Sb_8$, and $Mg_3Zn_3Yb_6Sb_8$.

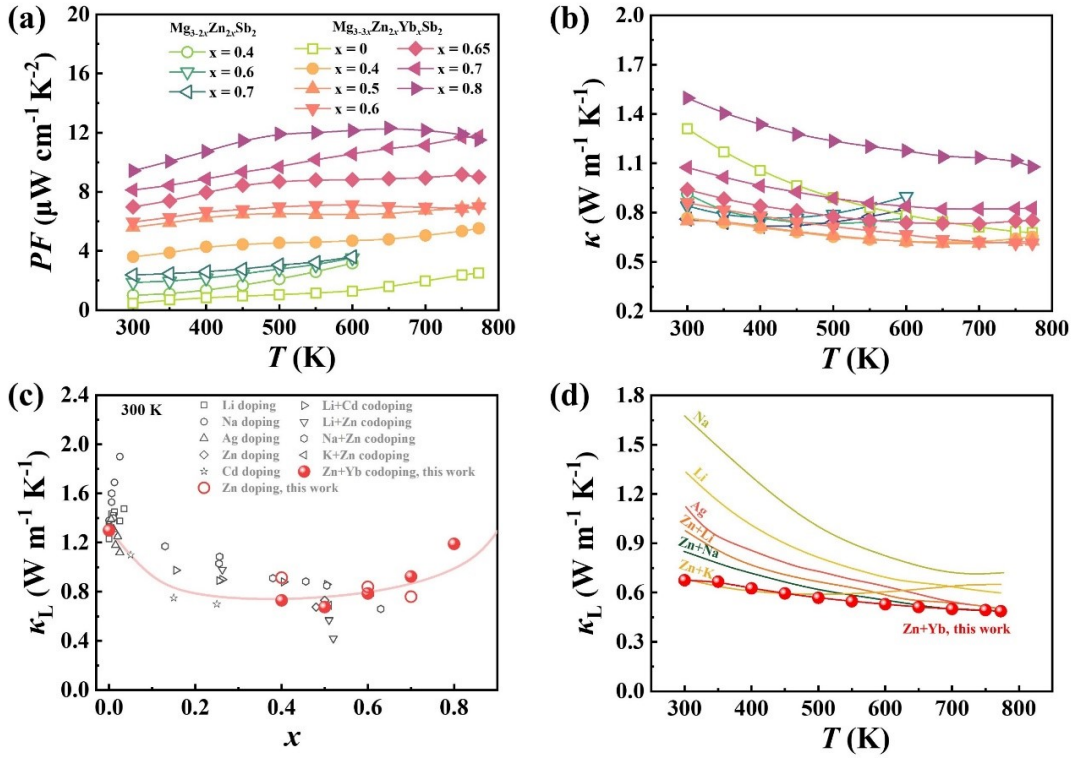

Figure S4. Temperature dependent **(a)** power factor and **(b)** thermal conductivity for $Mg_{3-2x}Zn_{2x}Sb_2$ (x = 0, 0.4, 0.6, 0.7) and $Mg_{3-3x}Zn_{2x}Yb_xSb_2$ (x = 0.4, 0.5, 0.6, 0.65, 0.7, 0.8). **(c)** Room temperature lattice thermal conductivity as a function of alloying content

x. The dashed lines are calculated by the Callaway model. The reported data are also included for comparison[3-8]. **(d)** Comparison of lattice thermal conductivity for $Mg_{3-3x}Zn_{2x}Yb_xSb_2$ (x = 0.5) with reported p-type Mg_3Sb_2-based materials[3-6, 8].

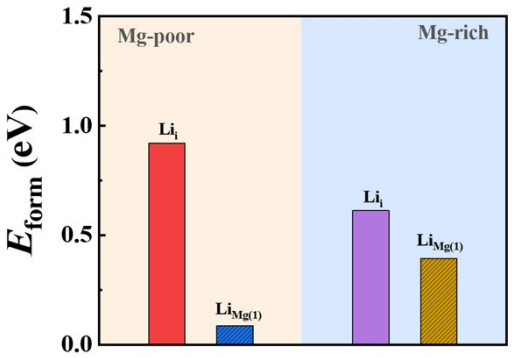

Figure S5. Defect formation energies of interstitial Li (Li_i) and substitutional Li at the Mg1 site ($Li_{Mg(1)}$) under Mg-poor and Mg-rich conditions.

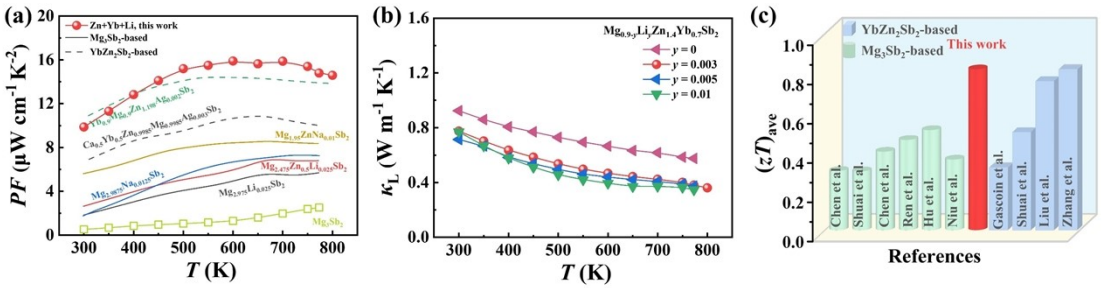

Figure S6. (a) Comparison of power factor for $Mg_{0.897}Li_{0.003}Zn_{1.4}Yb_{0.7}Sb_2$ and reported p-type Mg_3Sb_2-based as well as $YbZn_2Sb_2$-based materials[3, 4, 6, 9, 10]. **(b)** Temperature dependence of lattice thermal conductivity of Li doped samples. **(c)** Comparison of average zT from 300 to 773 K in the optimized p-type Mg_3Sb_2- and $YbZn_2Sb_2$-based materials[3-6, 9-13].

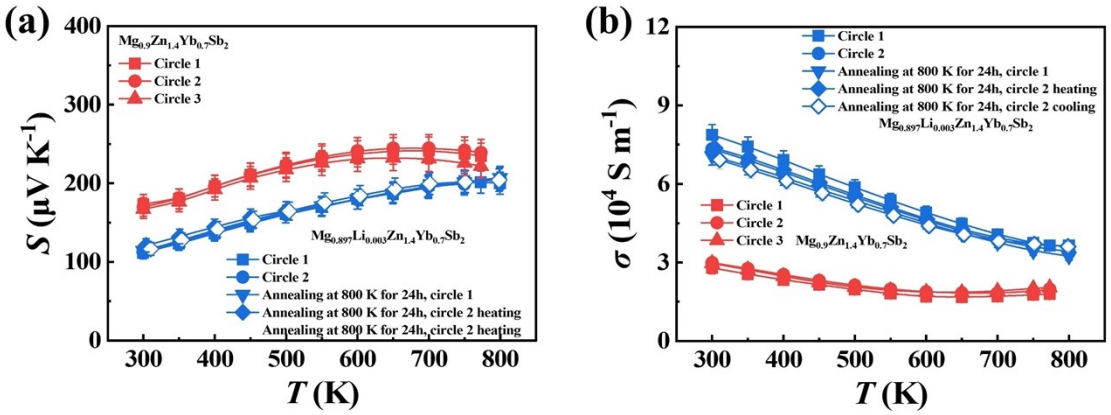

Figure S7. Repeatable tests on **(a)** Seebeck coefficient *S* and **(b)** electrical conductivity σ for $Mg_{0.9}Zn_{1.4}Yb_{0.7}Sb_2$ and $Mg_{0.897}Li_{0.003}Zn_{1.4}Yb_{0.7}Sb_2$.

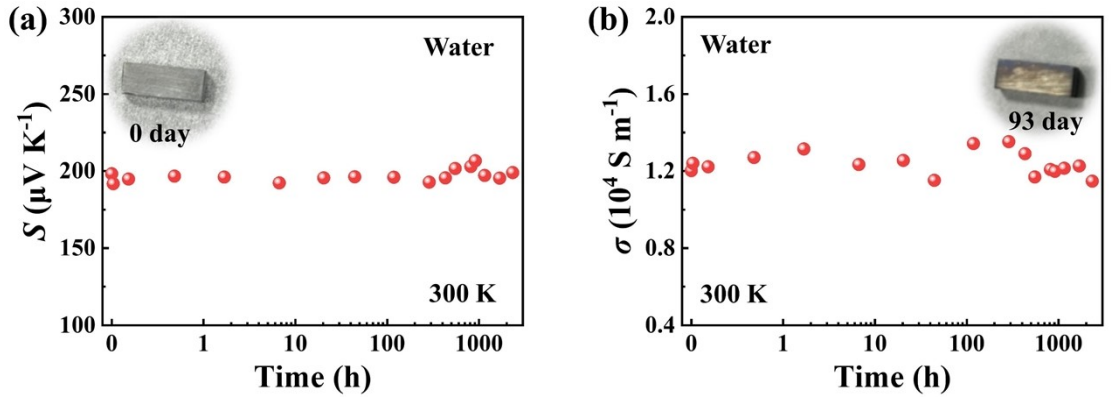

Figure S8. Chemical stable test in water of **(a)** Seebeck coefficient and **(b)** electrical conductivity for $Mg_{1.2}Zn_{1.2}Yb_{0.6}Sb_2$.

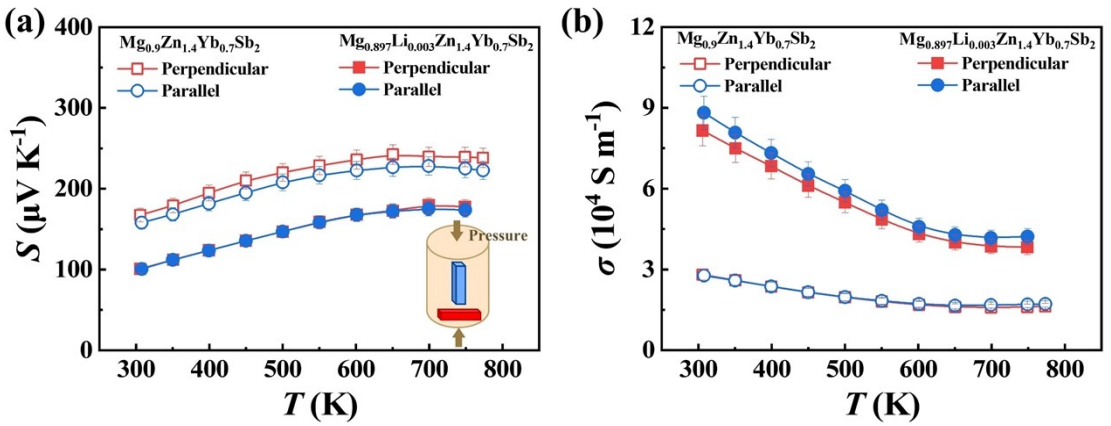

Figure S9. Temperature dependent **(a)** Seebeck coefficient and **(b)** electrical conductivity in directions perpendicular and parallel to the sintering pressure for $Mg_{0.9}Zn_{1.4}Yb_{0.7}Sb_2$ (hollow) and $Mg_{0.897}Li_{0.003}Zn_{1.4}Yb_{0.7}Sb_2$ (solid). The slight disparity

in electrical properties between the perpendicular and parallel directions falls within the measurement uncertainties.

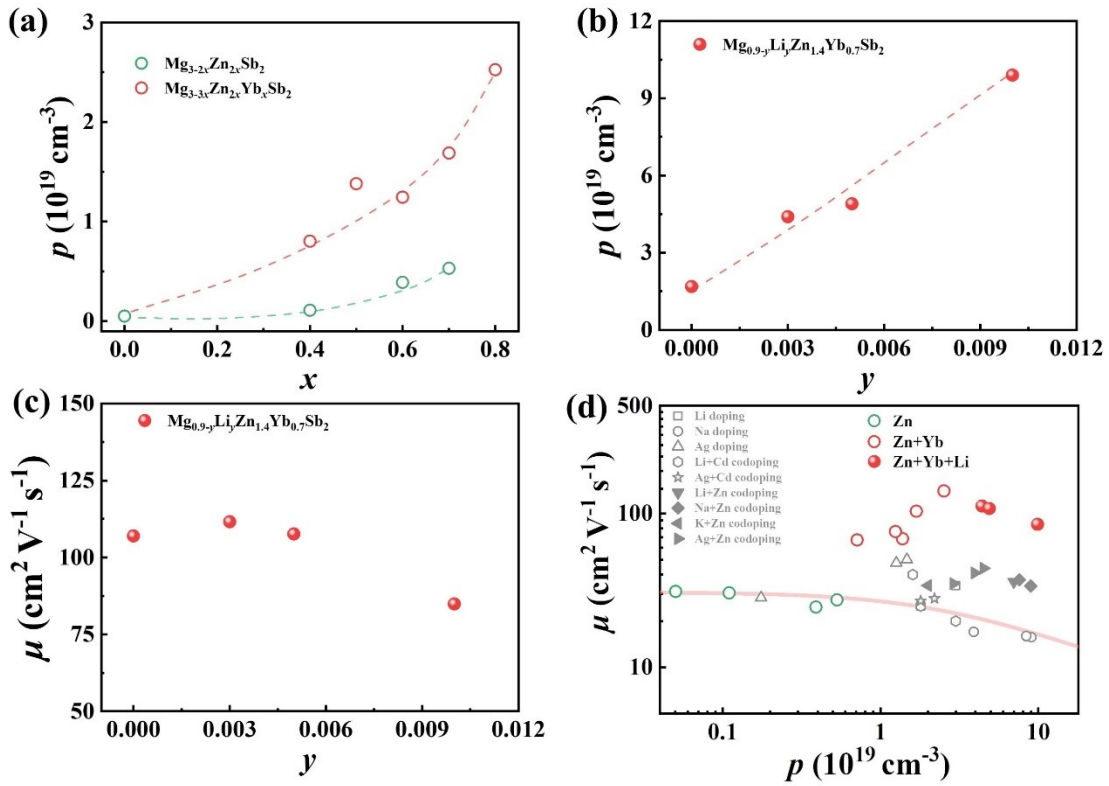

Figure S10. (a) Room temperature carrier concentration as a function of x for $Mg_{3-2x}Zn_{2x}Sb_2$ (x = 0, 0.4, 0.6, 0.7) and $Mg_{3-3x}Zn_{2x}Yb_xSb_2$ (x = 0.4, 0.5, 0.6, 0.7, 0.8). **(b)** Room Hall carrier concentration and **(c)** carrier mobility for $Mg_{0.9-y}Li_yZn_{1.4}Yb_{0.7}Sb_2$ (y = 0, 0.003, 0.005, 0.01). The dashed lines are guide to the eyes. **(d)** Room temperature carrier mobility *versus* carrier concentration for p-Mg_3Sb_2-based materials. The reported data of Mg_3Sb_2-based materials are included for comparison[3-8, 14]. The red solid line is calculated by the SPB model with an effective mass 0.65 m_e.

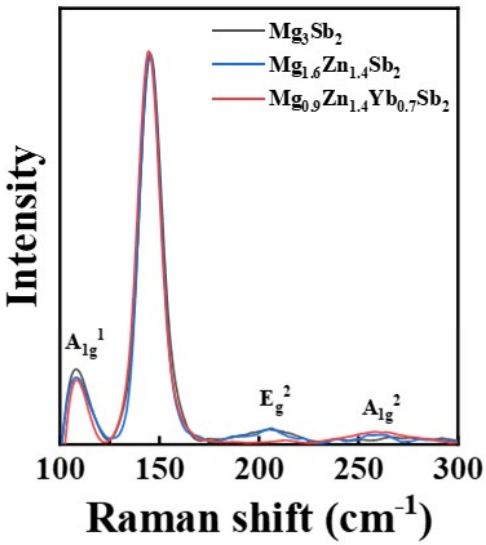

Figure S11. Room-temperature Raman spectra for $Mg_{3-2x}Zn_{2x}Sb_2$ (x = 0, 0.7) and $Mg_{3-3x}Zn_{2x}Yb_xSb_2$ (x = 0.7). The $P\bar{3}m1$ space group theoretically includes eight optical modes, in which four modes ($2A_{1g}+2E_g$) are Raman-active and four modes ($2A_{2u}+2E_u$) are infrared-active[15]. We can recognize three Raman active peaks in the range of 100 – 300 cm^{-1}. They occur at 110, 206, and 259 cm^{-1} in wavenumber, corresponding to the A_{1g}^1, E_g^2, and A_{1g}^2 vibration mode. The unexpected peak at 145 cm^{-1} was supposed to be the detection of the zone edged acoustic phonon modes, which has also been observed in previous reports[16-18]. These high-intensity Raman active peaks response the high-quality crystallographic morphology of our solid solutions.

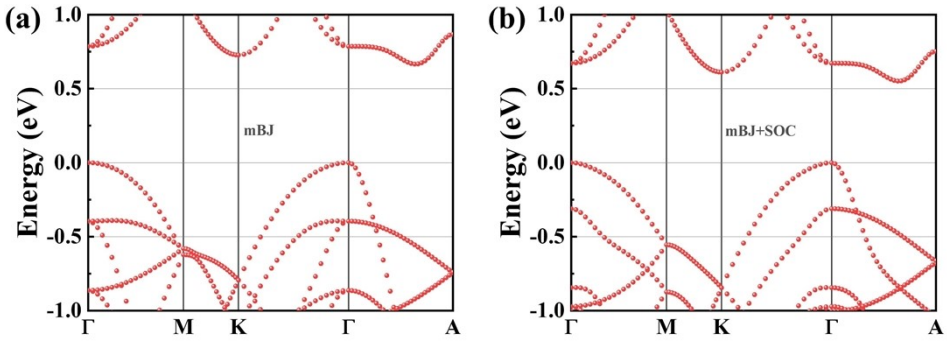

Figure S12. Comparison of the band structures for Mg_3Sb_2 without and with SOC.

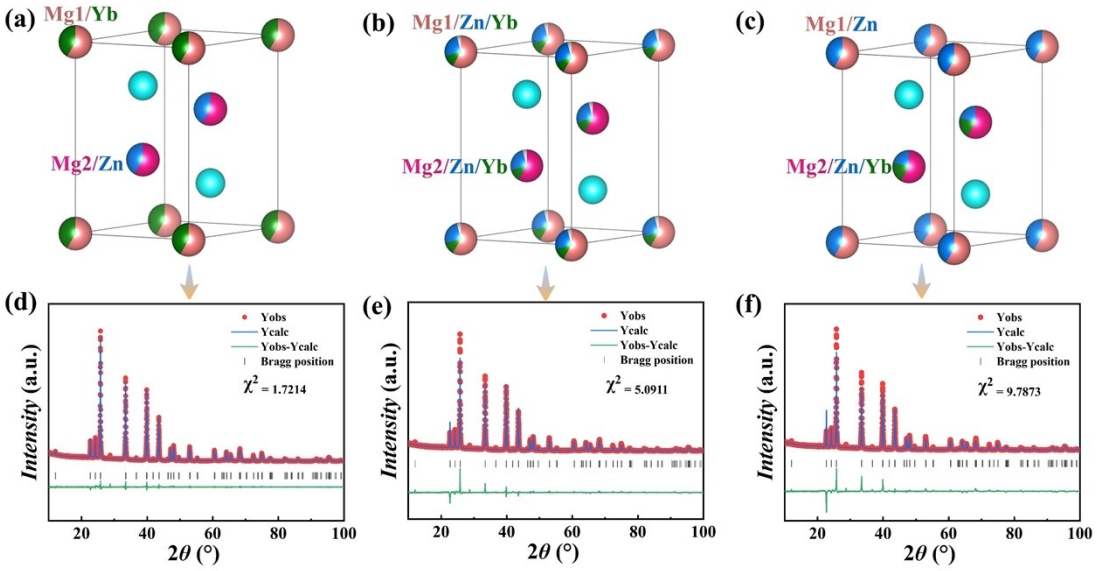

Figure S13. Illustration of crystal structures of three different model and the corresponding Rietveld refinement results for $Mg_{3-3x}Zn_{2x}Yb_xSb_2$ (x = 0.4). **(a, d)** model (i): Zn and Yb respectively replace Mg2 (2*d*) and Mg1 (1*a*) positions; **(b, e)** model (ii): Zn and Yb randomly reside on both Mg1 and Mg2 positions; **(c, f)** model (iii): Yb reside only on the Mg2 (2*d*) while Zn could distribute on both Mg1 (1*a*) and Mg2 (2*d*) positions.

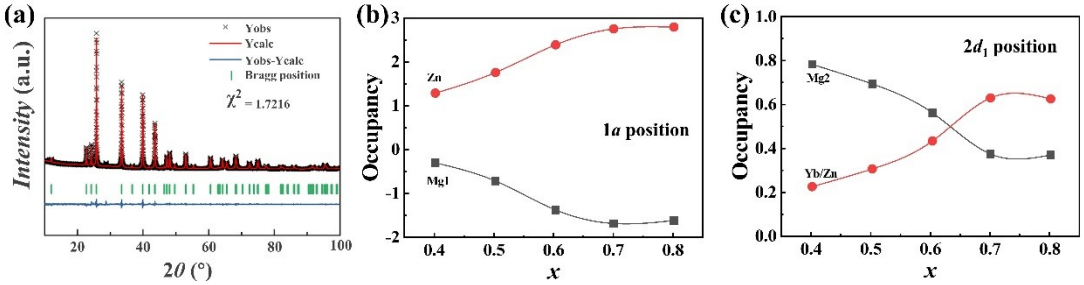

Figure S14. Rietveld refinement results for $Mg_{3-3x}Zn_{2x}Yb_xSb_2$ (x = 0.4) with the atom occupancy relaxed in model (iii). **(a)** Overlaid calculated pattern with difference profile below. **(b)** Atom occupancies of Mg1/Zn at 1*a* position and **(c)** Mg2/(Yb/Zn) at $2d_1$ position.

Table S1. Calculated effective mass of the holes at the valence band (VB) maximum along different directions (m^*_{xx}, m^*_{yy}, m^*_{zz}) and single valley effective mass m^*_b.

Content	Method	VB	$m^*_{xx}/(m_e)$	$m^*_{yy}/(m_e)$	$m^*_{zz}/(m_e)$	$m^*_b/(m_e)$
$Mg_{12}Sb_8$	mBJ	VB1	1.1	1.1	0.09	0.48
		VB2	0.14	1.46	1.63	0.69
		VB2	0.14	0.14	1.63	0.32
$Mg_{12}Sb_8$	mBJ+ SOC	VB1	0.92	0.89	0.09	0.42
		VB2	0.23	0.23	1.59	0.44
$Mg_{10}Zn_2Sb_8$		VB1	0.99	0.98	0.10	0.46
		VB2	0.20	0.20	1.19	0.36
$Mg_8Zn_4Sb_8$		VB1	1.10	1.04	0.09	0.47
		VB2	0.15	0.26	0.75	0.31
$Mg_6Zn_6Sb_8$		VB1	0.85	0.59	0.13	0.40
		VB2	0.13	0.13	0.81	0.24
$Mg_9Zn_2Yb_1Sb_8$		VB1	0.80	0.82	0.11	0.42
		VB2	0.19	0.19	0.98	0.33
$Mg_6Zn_4Yb_2Sb_8$		VB1	0.67	0.78	0.08	0.35
		VB2	0.18	0.16	0.27	0.20
$Mg_3Zn_6Yb_3Sb_8$		VB1	0.43	0.44	0.09	0.26
		VB2	0.11	0.11	0.35	0.16

Table S2. The lattice parameters derived from Rietveld refinement for $Mg_{3-2x}Zn_{2x}Sb_2$ (x = 0, 0.4, 0.6, 0.7).

	$x = 0$	$x = 0.4$	$x = 0.6$	$x = 0.7$
Space group	$P\bar{3}m1$	$P\bar{3}m1$	$P\bar{3}m1$	$P\bar{3}m1$
a (Å)	4.5607	4.4750	4.4582	4.4521
c (Å)	7.2291	7.2069	7.2029	7.2034

V (Å^3)	130.220	124.989	123.982	123.652

Table S3. The lattice parameters derived from Rietveld refinement for $Mg_{3-3x}Zn_{2x}Yb_xSb_2$ (x = 0.4, 0.5, 0.6, 0.7, 0.8).

	x = 0.4	x = 0.5	x = 0.6	x = 0.7	x = 0.8
Space group	$P\bar{3}m1$	$P\bar{3}m1$	$P\bar{3}m1$	$P\bar{3}m1$	$P\bar{3}m1$
a (Å)	4.5204	4.5147	4.5332	4.5113	4.4840
c (Å)	7.3462	7.3745	7.4366	7.4438	7.4396
V (Å^3)	130.001	130.175	132.345	131.199	129.542

Reference

1. Y. Pei, A. D. LaLonde, H. Wang and G. J. Snyder, *Energy Environ. Sci.*, 2012, **5**, 7963-7969.
2. J. Zhang, L. Song, S. H. Pedersen, Y. Hao, T. H. Le and B. I. Bo, *Nat. Commun.*, 2017, **8** 13901
3. C. Chen, X. Li, S. Li, X. Wang, Z. Zhang, J. Sui, F. Cao, X. Liu and Q. Zhang, *J. Mater. Sci.*, 2018, **53**, 16001-16009.
4. J. Hu, J. Zhu, F. Guo, H. Qin, Y. Liu, Q. Zhang, Z. Liu, W. Cai and J. Sui, *Research*, 2022, **2022**, 9842949.
5. Y. Niu, C. Yang, T. Zhou, Y. Pan and C. Wang, *ACS Appl. Mater. Interfaces*, 2020, **12**, 37330-37337.
6. J. Shuai, Y. Wang, H. Kim, Z. Liu, J. Sun, S. Chen, J. Sui and Z. Ren, *Acta. mater.*, 2015, **93**, 187-193.
7. S. Xiao, K. Peng, Z. Zhou, H. Wang, S. Zheng, X. Lu, G. Han, G. Wang and X. Zhou, *J. Magnes. Alloy*, 2021.
8. L. Song, J. Zhang and B. B. Iversen, *J. Mater. Chem. A*, 2017, **5**, 4932-4939.
9. K.-J. Liu, Z.-W. Zhang, C. Chen, L.-H. Wei, H.-L. He, J. Mao and Q. Zhang, *Rare Met.*, 2022, **41**, 2998-3004.
10. Z. Zhang, Y. Yan, X. Li, X. Wang, J. Li, C. Chen, F. Cao, J. Sui, X. Lin, X. Liu, G. Xie and Q. Zhang, *Adv. Energy Mater.*, 2020, **10**, 2001229.
11. Z. Ren, J. Shuai, J. Mao, Q. Zhu, S. Song, Y. Ni and S. Chen, *Acta. mater.*, 2018, **143**, 265-271.
12. F. Gascoin, S. Ottensmann, D. Stark, S. M. Haïle and G. J. Snyder, *Adv. Funct. Mater.*, 2005, **15**, 1860-1864.
13. J. Shuai, Y. Wang, Z. Liu, H. S. Kim, J. Mao, J. Sui and Z. Ren, *Nano Energy*, 2016, **25**, 136-144.
14. L. Huang, T. Liu, X. Mo, G. Yuan, R. Wang, H. Liu, X. Lei, Q. Zhang and Z. Ren, *Mater. Today Phys.*, 2021, **21**, 100564.
15. X. Ma, H. Yao, S. Zhi, P. Zhao, S. Ye, S. Duan, L. Yin, J. Li, X. Bao, J. Sui, F. Cao, Q. Zhang and J. Mao, *Chem. Mater.*, 2023, **35**, 5640-5647.
16. A. Bhardwaj, A. K. Shukla, S. R. Dhakate and D. K. Misra, *RSC Adv.*, 2015, **5**, 11058-11070.
17. M. Jin, S. Lin, W. Li, X. Zhang and Y. Pei, *Mater. Today Phys.*, 2021, **21**, 100508.
18. Z. Liu, N. Sato, W. Gao, K. Yubuta, N. Kawamoto, M. Mitome, K. Kurashima, Y. Owada, K.

Nagase, C.-H. Lee, J. Yi, K. Tsuchiya and T. Mori, *Joule*, 2021, **5**, 1196-1208.